Article

Effects of Covalency on Anionic Redox Chemistry in Semiquinoid-Based Metal–Organic Frameworks

Michael E. Ziebel, Carlo Alberto Gaggioli, Ari B. Turkiewicz, Won Ryu, Laura Gagliardi, and Jeffrey R. Long*

ACCESS | Metrics & More | Article Recommendations | Supporting Information

ABSTRACT: Two iron−semiquinoid framework materials, $(H_2NMe_2)_2Fe_2(Cl_2 \, dhbq)_3$ (**1**) and $(H_2NMe_2)_4Fe_3(Cl_2 \, dhbq)_3(SO_4)_2$ ($Cl_2 \, dhbq^{n-}$ = deprotonated 2,5-dichloro-3,6-dihydroxybenzoquinone) (**2-SO₄**), are shown to possess electrochemical capacities of up to 195 mAh/g. Employing a variety of spectroscopic methods, we demonstrate that these exceptional capacities arise from a combination of metal- and ligand-centered redox processes, a result supported by electronic structure calculations. Importantly, similar capacities are not observed in isostructural frameworks containing redox-inactive metal ions, highlighting the importance of energy alignment between metal and ligand orbitals to achieve high capacities at high potentials in these materials. Prototype lithium-ion devices constructed using **1** as a cathode demonstrate reasonable capacity retention over 50 cycles, with a peak specific energy of 533 Wh/kg, representing the highest value yet reported for a metal−organic framework. In contrast, the capacities of devices using **2-SO₄** as a cathode rapidly diminish over several cycles due to the low electronic conductivity of the material, illustrating the nonviability of insulating frameworks as cathode materials. Finally, **1** is further demonstrated to access similar capacities as a sodium-ion or potassium-ion cathode. Together, these results demonstrate the feasibility and versatility of metal−organic frameworks as energy storage materials for a wide range of battery chemistries.
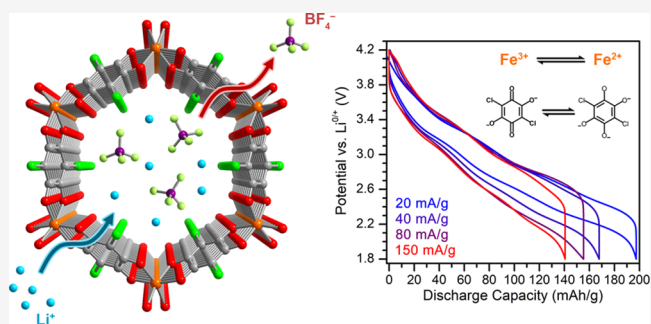
INTRODUCTION

Cathode materials for lithium-ion batteries typically rely on transition metal-based redox couples, such as $Fe^{II/III}$ in $LiFePO_4$ and $Co^{III/IV}$ in $LiCoO_2$. Despite the prevalence of these materials, their use of single electron redox couples imposes a fundamental limitation on the specific capacities that can be achieved in energy storage devices.[1] In efforts to surmount this limitation, record capacities have recently been achieved in oxide materials through utilization of anionic redox processes, where partial oxidation of the bridging oxygen ligands substantially increases the charge capacity of the material.[2] However, the formation of oxygen−oxygen bonds in these materials at high potentials can lead to the release of O_2 gas, which forms an insulating layer that inhibits electrochemical cycling.[3] Furthermore, these anionic redox processes are typically associated with large potential polarizations, sluggish kinetics, and substantial voltage fade after repeated cycling.[4] As such, commercialization of cathode materials that function based on anionic redox processes requires the use of ligands that provide increased structural and electrochemical stability in devices.[5]

The highly tunable geometric and electronic structures of metal−organic frameworks provides an intriguing template to achieve high capacity cathodes based on anionic redox activity.[6] In the vast majority of metal−organic frameworks, a low mass percent of metal ions and a large mass percent of redox-inert ligands typically yields specific capacities far lower than those found in dense inorganic solids.[7] However, incorporation of redox-active organic linkers into these frameworks can enable simultaneous utilization of metal-based and ligand-based redox processes to achieve capacities that meet or exceed those of traditional cathode materials. In addition, the void spaces intrinsic to metal−organic frameworks could also facilitate rapid transport of cations or anions, thereby enabling faster kinetics than those found in conversion or intercalation electrodes.[8] Furthermore, because the mobile cationic species can be shielded from the framework by solvent molecules within the pore, cathode materials based on metal−organic frameworks could address some of the challenges facing next-generation battery technologies, such as sodium-ion and magnesium-ion chemistries.[9]
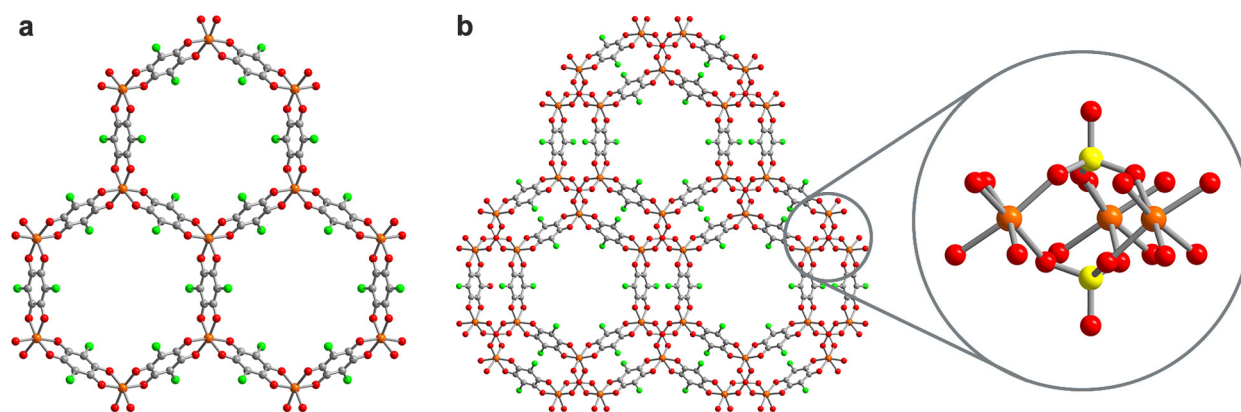
Figure 1. Structures of a single two-dimensional layer of **1** (a) and **2-SO₄** (b), as viewed down the *c*-axis. The enlarged window depicts the $Fe_3(SO_4)_2$ building unit, as viewed normal to the *c*-axis. Orange, gray, red, yellow, and green spheres represent Fe, C, O, S, and Cl atoms, respectively. Solvent and dimethylammonium cations are omitted for clarity. The two-dimensional layers of both phases are eclipsed, resulting in a one-dimensional channel along the *c*-axis.

Recently, several metal−organic materials have been shown to display competitive specific capacities via anionic redox activity, but these systems suffer from major limitations that preclude their utilization in practical devices. For example, the framework Cu(aqdc) (aqdc²⁻ = 2,7anthraquinonedicarboxylate) achieves capacities approaching 160 mAh/g by utilizing metal- and ligand-centered redox chemistry, but the material is electronically insulating and therefore requires the use of very slow charging rates and a large quantity of a conductive additive.[10] The two phases of the coordination solid Cu-(TCNQ) (TCNQ⁻ = tetracyanoquinodimethane monoanion) are conductive and can achieve capacities up to 250 mAh/g, but their nonporous structure hinders anion insertion during oxidation, resulting in dissociation into free Cuᴵᴵ ions and neutral TCNQ ligands or conversion to a new phase with low Coulombic efficiency.[11] Finally, Co₃(hib)₂ (hib³⁻ = hexaiminobenzene) achieves capacities of 250 mAh/g at rapid charging rates, but the low potential required to fully reduce the ligand limits its specific energy as a cathode material.[12]

From these examples, several design criteria can be identified for metal−organic framework cathodes utilizing anionic redox processes. First, the material must possess reasonable electronic conductivity (>10⁻⁵ S/cm) and should ideally be much more conductive. Second, the material should possess pores and pore windows large enough to insert both the cations and the anions present in the electrolyte. Finally, the redox activity of the organic linker must be accessible at high potentials to achieve devices with sufficient energy density for practical applications.

Identifying framework materials that meet all three of these criteria is challenging, largely because the factors influencing the conductivity and electrochemical properties of metal−organic frameworks are still poorly understood.[13] Herein, we report the electrochemical behavior of two iron−semiquinoid frameworks that combine metal- and ligand-centered redox activity to achieve large electrochemical capacities at high potentials. Further, we demonstrate that this redox activity is unique among structurally similar frameworks, revealing that partial reduction of the iron centers stabilizes the fully reduced state of the ligand. Prototype devices based on these materials achieve high capacity retention over 50 cycles and at current densities up to 150 mA/g.

RESULTS AND DISCUSSION

Syntheses and Structures. The design of a framework material that is capable of achieving large capacities through anionic redox chemistry requires careful consideration of the framework structure and bonding. While incorporation of redox-active organic moieties into a framework structure is now relatively common, most examples of this approach are found in insulating frameworks that exhibit slow transport of electrons to the redox-active sites.[10,14] In contrast, to achieve reversible ligand-centered redox chemistry in a bulk material, the organic linker must be placed in direct conjugation with metal centers or other organic linkers to develop a long-range conduction pathway. Toward this end, molecules based on 2,5-dihydroxybenzoquinone (H₂ dhbq) and its derivatives represent a particularly promising family of organic linkers. Indeed, frameworks synthesized from these ligands can display electronic conductivity in which d-π conjugation facilitates charge hopping between mixed-valent ligand centers.[15] Notably, the three redox states of this ligand are readily accessible in molecular transition metal complexes, such that each ligand can, in principle, contribute two electrons to the capacity of these frameworks.[16]

We previously reported the electrochemical behavior of the three-dimensional framework material (NBu₄)₂Fe₂(dhbq)₃, in which two nets of opposite chirality are interpenetrated and locked in place by tetrabutylammonium cations.[15b] Assuming full accessibility of metal- (Feᴵᴵ/ᴵᴵᴵ) and ligand-centered (dhbq²/³/⁴⁻) redox processes, this material would possess a capacity of eight electrons per formula unit. While cyclic voltammetry revealed two quasi-reversible reduction events for this material, oxidation of the parent framework was unsuccessful due to the poor mobility of the bulky cations. Furthermore, the dense packing of the structure resulted in poor Coulombic efficiencies and limited capacity retention with repeated cycling. To better access the full electrochemical capacity of this metal−ligand pairing, we turned to the two-dimensional structural isomer (H₂NMe₂)₂Fe₂(Cl₂ dhbq)₃·*n*DMF(**1**), which features smaller dimethylammonium cations and is permanently porous via its hexagonal one-dimensional channels (Figure 1).[17] The material was obtained using a synthesis similar to those reported for the chromium and aluminum analogues, starting from Fe(NO₃)₃ and using in situ-generated dimethylammonium formate as the ligand reduc-

tant.[15e,18] This method yields a crystalline black solid with unit cell parameters similar to those for the material prepared using the reported synthesis (Figure S1 of the Supporting Information, SI). The infrared spectrum of **1** is consistent with the previously reported electronic structure of $(H_2NMe_2)_2Fe^{III}_2(Cl_2 \ dhbq^{2-})(Cl_2 \ dhbq^{3-})_2$ (Figure S6).[17]

During our pursuit of new synthetic conditions for **1**, we also discovered the unreported phase $(H_2NMe_2)_4Fe_3(Cl_2 \ dhbq)_3(SO_4)_2 \cdot nDMF$ (**2-SO_4**), which was isolated from the reaction of $Fe(SO_4) \cdot 7H_2O$ with chloranilic acid. Single-crystal X-ray diffraction revealed that this phase forms a two-dimensional, double-walled honeycomb structure with hexagonal channels similar to those observed in **1**. In **2-SO_4**, each iron center is coordinated by two chloranilate ligands and two μ_3-SO_4^{2-} groups to form a $Fe_3(SO_4)_2$ building unit (Figure 1). Similar incorporation of sulfate ions into an iron−catecholate framework was previously observed.[19] In contrast to **1**, Mössbauer spectroscopy revealed incomplete metal-to-ligand electron transfer in **2-SO_4**, with nearly one-third of the iron ions remaining divalent in character (Figure S8). Notably, while both metal and ligand mixed-valency exist in **2-SO_4**, this material lacks the infinite connectivity of iron and chloranilate ligands that promote conductivity and magnetic ordering in **1**.[15c,17] Consistent with this structure, the pressed-pellet conductivity of **2-SO_4** is only 8.4×10^{-5} S/cm, two to three orders of magnitude lower than that of **1** (Figure S9). Unlike that in **1**, in which d-π conjugation facilitates long-range charge hopping, the electronic conductivity in **2-SO_4** is limited by weak $\pi-\pi$ orbital overlap between chloranilate linkers or charge hopping mediated by the more ionic sulfate ligands. Interestingly, the intervalence charge transfer absorption bands observed for **1** and **2-SO_4** display similar bandwidths and appear at nearly identical energies, suggesting that this excitation is a localized electronic transition between two linkers with different oxidation states, rather than one associated with long-range charge transfer (Figure S10).[20] This result indicates that conductivity in **1** likely arises from localized charge hopping, as opposed to band-like transport. More generally, this result demonstrates that high conductivities can be achieved in metal−organic frameworks in the absence of band-like transport.

Electrochemical Behavior. To probe the electrochemical behavior of **1** and **2-SO_4**, we carried out slow-scan cyclic voltammetry (Figure 2). As expected, the hexagonal pores and smaller cations of these phases enable reversible oxidation to the neutral frameworks via removal of dimethylammonium cations, unlike the irreversible or inaccessible oxidation observed in the two- or three-dimensional phases with larger cations.[15b,21] In **1**, redox processes centered at $E_{1/2}$ = 2.71 and 3.25 V vs $Li^{0/+}$ correspond to reversible reduction of $Cl_2 \ dhbq^{2-}$ and oxidation of $Cl_2 \ dhbq^{3-}$, (i.e., the $Cl_2 \ dhbq^{2/3-}$ redox couple). The initial reduction in **1** has been previously studied through chemical methods, which demonstrated that it is entirely ligand-centered in character.[15c] The two observed processes each correspond to a one-electron reduction or oxidation of half the linkers in **1**. Although solid-state electrochemical measurements likely overestimate comproportionation constants, the separation of these features corresponds to a $K_c \approx 1.3 \times 10^9$ for **1**, consistent with the short-range electron delocalization observed spectroscopically.[22] The cyclic voltammogram of **2-SO_4** also displays processes corresponding to the same ligand-based redox couple, although the oxidative redox events for **2-SO_4** appear as multiple
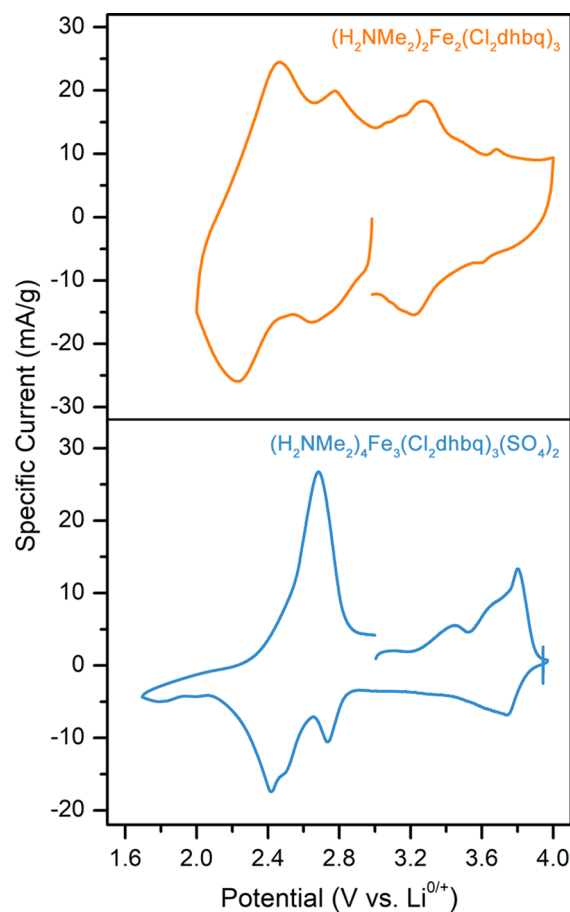

Figure 2. Solid-state cyclic voltammograms of **1** (top) and **2-SO_4** (bottom), collected at 30 μV/s with lithium counter and reference electrodes and a 0.1 M $LiBF_4$ electrolyte solution.

features at a much higher potential ($E_{1/2}$ = 3.77 V vs $Li^{0/+}$), corresponding to the combined oxidation of Fe^{II} and $Cl_2 \ dhbq^{3-}$.

Excitingly, both **1** and **2-SO_4** display additional reversible reductions centered at $E_{1/2}$ = 2.35 and 2.5 V, respectively, which correspond to reduction of Fe^{III} or reduction of the linker beyond $Cl_2 \ dhbq^{3-}$. Integration of the reductive voltammograms for **1** and **2-SO_4** suggest that the combined redox processes endow the materials with large overall capacities of 6 and 8 electrons per formula unit (3 and 2.7 electrons per Fe) for **1** and **2-SO_4**, respectively. Notably, the electron capacity of **1** corresponds well to two electrons per linker, which initially suggested primarily ligand-centered redox activity. However, if the charge capacity of **1** stems entirely from its organic-based redox chemistry, then isostructural phases with this ligand should similarly possess large electrochemical capacities. While we previously demonstrated that the chromium analogue of **1** possesses an electronic structure similar to the iron phase and can be reduced electrochemically to $[Cr^{III}_2(dhbq^{3-})_3]^{3-}$, attempts to access Cr^{II} or $dhbq^{4-}$ at more reducing potentials resulted in irreversible redox processes.[15f] Furthermore, cyclic voltammograms of the aluminum and zinc phases display reversible processes only for the $dhbq^{2/3-}$ couple (Figure S11), and similar results were previously reported for analogous cadmium, iron, and mixed manganese−chromium phases with different charge-balancing cations.[21,23,24]

Given the accessibility of the dhbq^{4-} state in dinuclear complexes, the absence of further reductions in these non-iron materials is somewhat surprising, although the large negative charges of these frameworks at full reduction may account for this disparity.[16,25] Consequently, the accessibility of this relative excess of reduction in the iron phases is indicative of metal−ligand interactions that stabilize the tetraanionic state of the ligand and are not present for other metal ions. Indeed, among reported phases, only the highly covalent vanadium phase displays an electrochemical capacity approaching that of **1**, suggesting that energy alignment of metal and ligand orbitals in these systems may play a critical role in determining their electrochemical capacities.[15f] Consistent with this hypothesis, a similar effect is seen in some oxides, such as LiCoO$_2$, in which X-ray absorption spectroscopy has revealed that the formally Co$^{III/IV}$ redox couple involves substantial oxygen character due to the covalent nature of the metal−ligand interactions.[26] Along these lines, covalency in **1**, or at least matching between metal and ligand reduction potentials, may give rise to a ligand-centered reduction with a substantial contribution from iron-based orbitals.

To better understand the nature of the excess redox activity in the iron phases relative to their non-iron congeners, we turned to ex situ Mössbauer spectroscopy measurements of the electrochemically oxidized and reduced materials (see Experimental Details in the SI and Figures 3 and S8). As expected, in their fully oxidized state, both frameworks possess primarily high-spin Fe^{III} sites. The presence of slightly inequivalent Fe^{III} sites likely results from a distribution of cations and anions within the pores of both materials. In the case of **1**, the iron ions remain almost entirely trivalent in character when the framework is subsequently reduced back to its original charge state, although a small amount of Fe^{II} is also observed, possibly due to uneven electrochemical reduction of the sample (Figure S12). Upon full electrochemical reduction, both **1** (Figure 3) and **2-SO$_4$** (Figure S8) display substantial high-spin Fe^{II} character, roughly 35% and 66%, respectively, suggesting metal-centered reduction plays a role in increasing the capacity of these iron−semiquinoid phases. Despite the presence of metal-based mixed-valency, neither phase displays evidence for iron-based valence delocalization at high temperature, suggesting valence-trapping of the Fe^{II} sites in the reduced compounds.[15g] Notably, the extent of iron reduction observed in **1** and **2-SO$_4$** is not sufficient to explain the full electrochemical capacity of the materials, suggesting that metal and ligand reduction occur simultaneously. Furthermore, upon electrochemical reduction, ex situ infrared spectroscopy measurements reveal redshifts in the quinone stretching frequencies with ν_{CO} = 1417 and 1412 cm^{-1} for **1** and **2-SO$_4$**, respectively, consistent with partial ligand reduction to the tetraanionic state. The ex situ UV−vis−NIR spectrum of reduced **1** reveals the disappearance of a metal-to-ligand charge transfer band at 18 000 cm^{-1}, due to the filling of ligand-based orbitals (Figures 4 and S6). On the basis of these results, the redox states of the materials in the reduced states can be formally assigned as $[Fe^{II}_{0.7}Fe^{III}_{1.3}(Cl2dhbq^{3-})_{0.7}(Cl_2 dhbq4-)_{2.3}]^{6-}$ and $[Fe^{II}_2Fe^{III}(Cl_2 dhbq^{4-})_3(SO_4)_2]^{9-}$ for **1** and **2-SO$_4$**, respectively.

Although the partial iron reduction in these materials explains only a portion of their overall capacity, it is evident that this metal-centered reduction is intimately linked to the stabilization of the tetraanionic ligand. Indeed, the orbital energies of the iron ions should increase upon partial
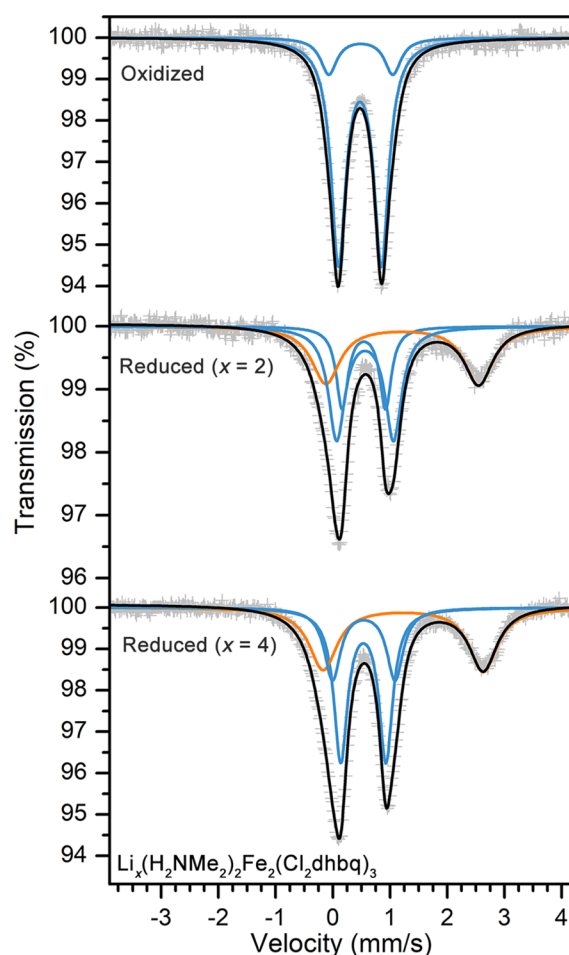

Figure 3. Mössbauer spectra of **1** at full oxidation and varying levels of reduction, where x corresponds to Li$_x$(H$_2$NMe$_2$)$_2$Fe$_2$(Cl$_2$ dhbq)$_3$. Gray crosses correspond to experimental data, while black, blue, and orange lines correspond to overall fits, fits of high-spin Fe^{III} sites, and fits of high-spin Fe^{II} sites, respectively. All spectra were recorded at 100 K. A full list of fit parameters can be found in Table S3.

reduction, potentially facilitating improved ligand-to-metal charge transfer interactions that stabilize the reduced ligand. Interestingly, Mössbauer spectroscopy of partially reduced samples of **1** revealed that the extent of Fe^{II} character remains nearly constant over the range x = 2−4 in Li$_x$(H$_2$NMe$_2$)$_2$Fe$_2$(Cl$_2$ dhbq)$_3$, suggesting that a small amount of metal-centered reduction may trigger the subsequent ligand-centered reduction (Figures 3 and S13). We note that ligand reduction to the tetraanionic state was not observed in a related framework with fully Fe^{II} character, suggesting that the similar reduction potentials of the metal and ligand plays a larger role in stabilizing this state than the presence of Fe^{II}.[24]

Electronic Structure Calculations. The initial reduction of **1** is expected to be entirely ligand-centered, based on our previously reported molecular orbital model for the framework and corresponding experimental data.[15c,f] However, this model predicts subsequent reductions to be primarily metal-centered, in contrast to the above spectroscopic analysis. This discrepancy suggests that a more complex bonding model is needed to fully understand and predict the true electrochemical behavior in these systems. Toward this end, further insight into the electronic structure of these systems was obtained from density functional theory (DFT) calculations
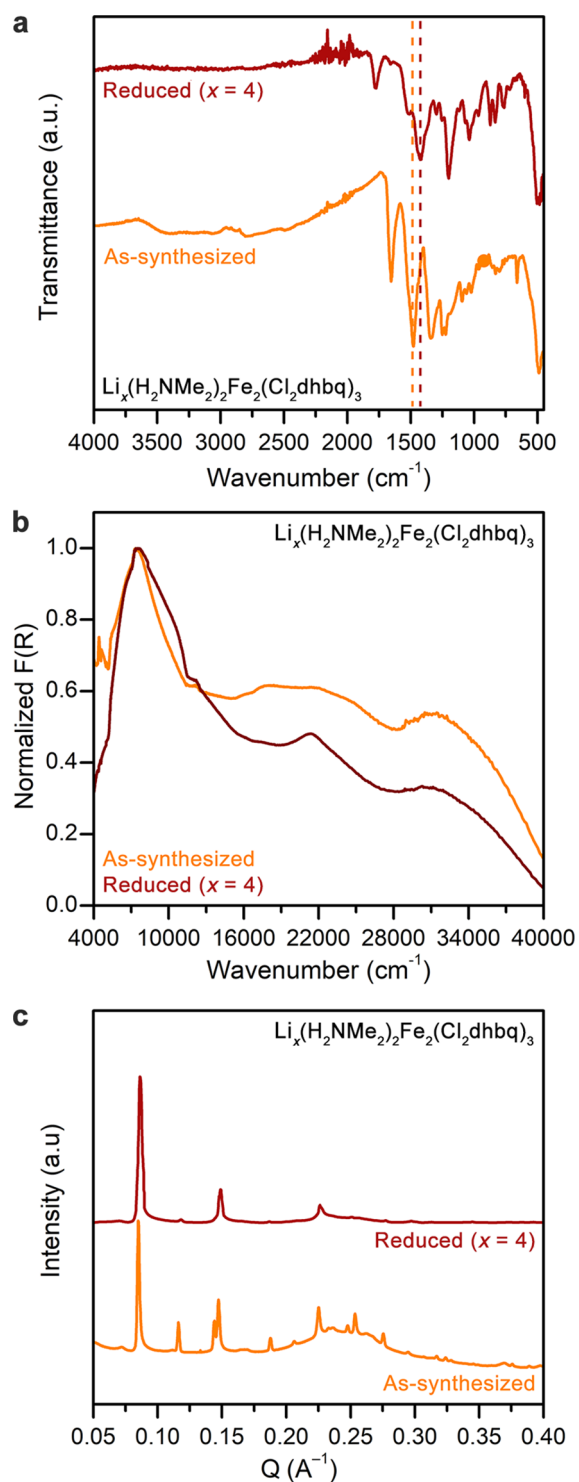
Figure 4. (a) Infrared spectrum for **1**, as-synthesized and at full reduction. Dashed lines highlight the quinone vibrational modes. Corresponding (b) UV−vis−NIR spectra and (c) powder X-ray diffraction patterns. The broad amorphous feature from $Q = 0.20–0.28$ Å^{-1} is due to the borosilicate capillary used during the measurement. A magnified diffraction pattern for reduced **1** can be found in Figure S7.

using the PBE+U method for a periodic unit cell of **1** and its chromium analogue. The negative charge of the framework unit cell was systematically increased to probe the localization of the added electron at each level of reduction, from the as-synthesized state to the four electron reduced state (unit cell

charge $n = -2$ to -6) (Table 1), and a uniform background charge field (with sufficient charge to maintain charge neutrality) was used to model the disordered cations in the pores of these frameworks.

Table 1. Cumulative Energy Gain (ΔE) for Simulated Reductions of Fe-Based 1 and the Isostructural Cr Phase, Calculated with PBE+U^a

Unit Cell Charge	ΔE, Fe (eV)	ΔE, Cr (eV)
−2	0.00	0.00
−3	−2.69 (−2.69)	−1.71 (−1.71)
−4	−4.67 (−1.98)	−2.68 (−0.97)
−5	−6.47 (−1.80)	−3.71 (−1.03)
−6	−7.43 (−0.96)	−4.43 (−0.72)

^{a}The numbers in parentheses correspond to the energy gained for each subsequent reduction.

Our calculations suggest that the first reduction ($n = -3$) of **1** is entirely ligand-centered, matching the experimental results. The second and third reductions ($n = -4$ and -5) were found to be most favorable as metal-centered reductions, while the fourth reduction ($n = -6$) was found again to be ligand-centered, with $[Fe^{II}_2(Cl_2\ dhbq^{3-})_2(Cl_2\ dhbq^{4-})]^{6-}$ representing the most stable configuration for the fully reduced state (Table S7). In all cases, the iron charge state was determined using the atomic spin density on the iron atoms. Electron density difference maps for ligand- and metal-centered reductions are depicted in Figures S14 and S15. The computational results are in agreement with the predictions generated from the molecular orbital model developed previously for **1**, but diverge from experimental results here that show substantial Fe^{III} character in the fully reduced framework. As such, we further modeled the reduced configurations by employing the HSE06 functional with a modified percentage of Hartree−Fock exchange.[27] With this functional, the first two reductions were found to be similar to the results using PBE+U, but the third and fourth reductions were found to be ligand-centered and metal-centered, respectively, indicating a change in the site localization of the intermediate reductions (Table S9). However, the most stable configuration for the fully reduced form was still observed to be exclusively Fe^{II} in character, and further attempts to model supercells of **1** revealed similar results.

Despite the disagreement with experiment, these results highlight the comparable energies of the Fe$^{II/III}$ and Cl$_2$dhbq$^{3/4-}$ couples, which likely play a role in explaining the accessibility of the highly reduced states in **1** and **2-SO$_4$**. Furthermore, the calculated Fe^{II} reduced states are highly localized on one iron site, in accord with the Mössbauer data (Figure S15). In contrast, all simulated reductions of the chromium analogue were found to be localized on the ligand, while attempts to computationally access a Cr^{II} structure consistently converged to a Cr^{III} structure with concomitant ligand reduction. A comparison of the energy gains (ΔE) for each subsequent reduction in the iron and chromium phases is shown in Table 1, where ΔE corresponds to the calculated energy difference between the reduced ($n-$) and as-synthesized ($2-$) phases. While ΔE is negative in all cases, due to the increasing number of electrons with reduction, the energy gains for each subsequent reduction should qualitatively reflect the relative ease of reduction in both systems. Notably, the energies of each subsequent reduction in the chromium
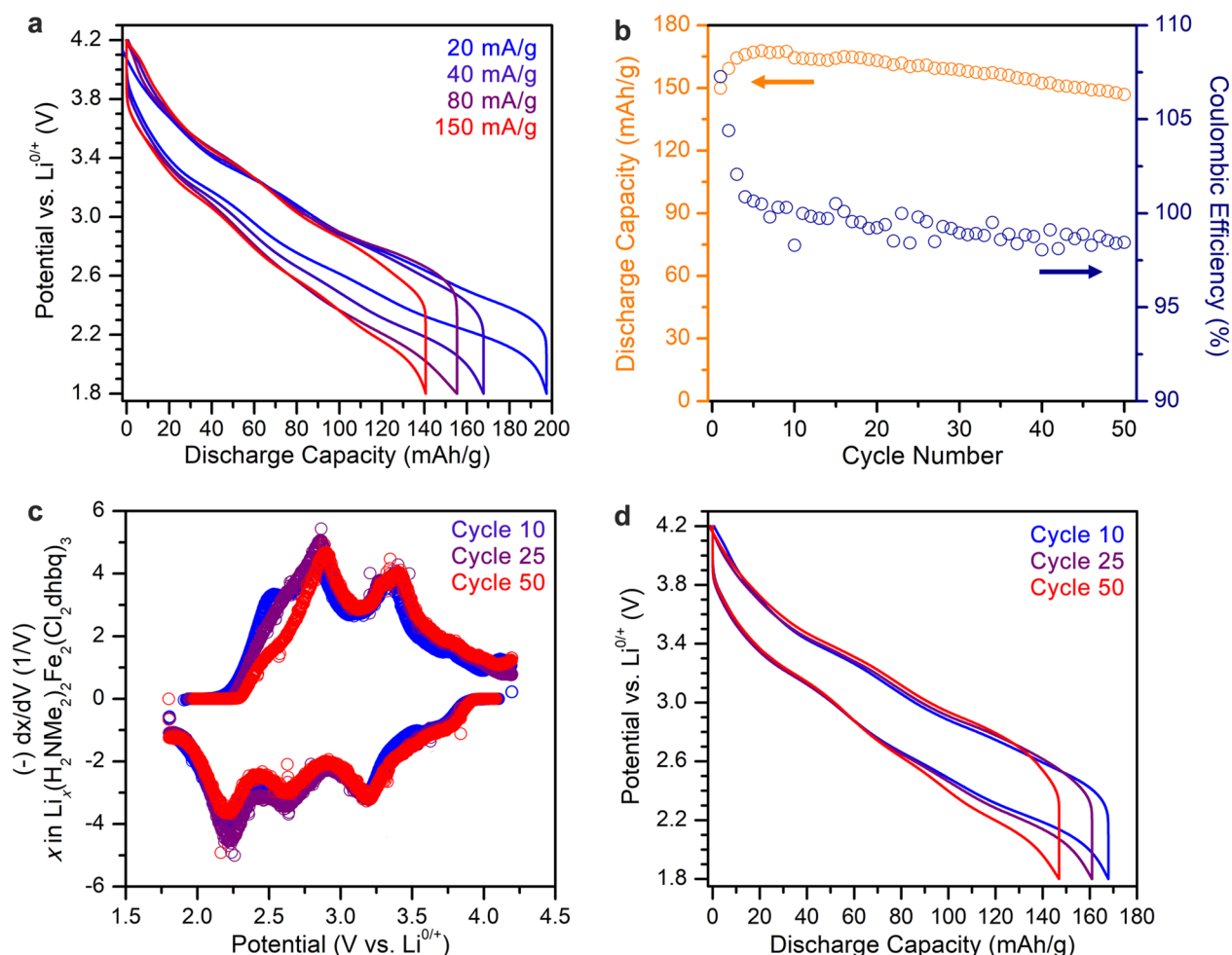
Figure 5. (a) Charge and discharge curves for **1** at various charging rates. Capacities over the first 15 cycles at each charging rate are depicted in Figure S17. (b) Discharge capacities and Coulombic efficiencies for **1** over 50 cycles at 40 mA/g. (c) Differential capacity profiles and (d) charge and discharge curves for **1** for cycle 10, 25, and 50 at 40 mA/g. The changing profile at the highest level of reduction indicates that full discharge may result in some material instability. Outlier points in the differential capacity profile have been removed for clarity.

phase were found to be less favorable than the corresponding energies for **1**. Furthermore, the cumulative energy gain for **1** for the reduction corresponding $n = 3-6$ was found to be 4.74 eV, compared to only 2.72 eV for the chromium phase. Thus, while the electronic structure of these simulated reductions does not perfectly match the experimental results, it demonstrates that the combined metal- and ligand-centered reduction of **1** plays a key role in enabling its large electrochemical capacity compared to other phases with the same ligand.

One possible explanation for the deviation between computations and experiment in these frameworks is a strong interaction between the framework and reductively inserted lithium cations. Ex situ powder X-ray diffraction of electrochemically reduced **1** reveals a slight contraction in the c-axis lattice spacing, despite the expected insertion of four solvated lithium cations (Figure 4). This contraction suggests that lithium ions may bridge two adjacent layers via coordination to the ligand oxygens. The charge polarization from this interaction could in turn stabilize a ligand-centered reduction more than predicted by the uniform charge distribution used in the electronic structure calculations above.

Cathode Performance. Iron-based cathode materials are highly sought due to the higher elemental abundance and

lower cost of iron compared to other commonly used metals, particularly cobalt and nickel.[28] Both **1** and **2-SO₄** possess capacities in excess of two electrons per transition metal ion, which suggests their potential viability as high-capacity cathode materials. Indeed, the electron capacities obtained from cyclic voltammetry correspond to theoretical capacities of 195 and 184 mAh/g, respectively, both of which exceed the specific capacity of $LiFePO_4$ (170 mAh/g).

To assess the potential cathode performance of **1** and **2-SO₄** in a Li-ion battery, we performed electrochemical cycling of both frameworks in lithium half-cells with a 0.1 M $LiBF_4$ propylene carbonate electrolyte. Because the as-synthesized frameworks are in a partially discharged state, all cycling experiments were preceded by a single precycle (discharged to 1.8 V and charged to 4.2 V) to reach a fully charged state (Figure S18). Reduced capacities were consistently observed for cells which were charged prior to an initial discharge, potentially related to exfoliation of the neutral material or increased anion insertion during the initial charge. The rate dependence of the discharge capacities for **1** and **2-SO₄** is shown in Figures 5 and S16. **2-SO₄** achieves a stable discharge capacity of only 165 mAh/g, representing 90% of the theoretical value, even at charging rates as low as 10 mA/g. With increased charging rates, the discharge capacity of **2-SO₄**

rapidly decreases, reaching a value of only 104 mAh/g (57% of theoretical) at 40 mA/g. Furthermore, at 40 mA/g, the electrochemical capacity of **2-SO$_4$** rapidly decreases, even over 15 cycles (Figure S17). This poor cathode performance of **2-SO$_4$** can likely be explained by its relatively low electronic conductivity, highlighting the limited utility of metal−organic frameworks with low conductivity in electrode applications.[10,14c,29] Sulfate loss upon reduction or lithium-ion trapping at sulfate sites could also contribute to poor cyclability in **2-SO$_4$**.

In contrast, the more conductive framework material **1** displays improved capacity retention at larger specific currents. For example, **1** achieves 100% of its theoretical capacity of 195 mAh/g up to 20 mA/g, and maintains capacities of 155 mAh/g (79% retention) at 80 mA/g and 141 mAh/g (72% retention) at 150 mA/g. At all charging rates, an increase in capacity is observed during the initial cycles, with Coulombic efficiencies exceeding 100% (Figure S17). This increase in capacity likely arises from a gradual deinsertion of bulky dimethylammonium cations, which enables improved transport of the mobile lithium species. The sloped discharge profile of **1**, in contrast to the staircase profile seen in many inorganic cathodes, is characteristic of a solid solution cathode. This classification is further supported by the ex situ powder X-ray diffraction pattern of the reduced material, which shows no evidence for a phase change upon reduction (Figure 4).[30] Notably, **1** achieves a peak specific energy of 533 Wh/kg at 20 mA/g, the highest yet reported for a metal−organic framework, and 386 Wh/kg at 80 mA/g (Figure S19).[31] The high energy output delivered by **1** is due to the relatively high potential of the final ligand reduction, particularly when compared to other frameworks achieving large capacities from highly reduced ligands.[12] Thus, both the charge capacity and energy density of **1** likely stem directly from the significant stabilization of the fully reduced ligand by covalent metal−ligand interactions.

To assess the long-term stability of **1**, we evaluated its discharge capacity over 50 cycles between 1.8 and 4.2 V at 40 mA/g (Figure 5). The capacity of **1** increases over the first 10 cycles, briefly stabilizing at 167 mAh/g, with peak gravimetric and volumetric energy densities of 453 Wh/kg and 445 Wh/L. The capacity and energy density then gradually decrease to 147 mAh/g (88% retention) and 403 Wh/kg (89% retention) by cycle 50, with Coulombic efficiencies ranging from 98 to 99.5%. Importantly, the high-potential (4.2 to 2.6 V) region of the discharge profiles for **1** remains nearly identical over 50 cycles, suggesting the framework does not degrade over the course of electrochemical cycling; rather, the decrease in capacity can be attributed primarily to the low-potential (2.6 to 1.8 V) region, in which combined metal and ligand reduction occurs (Figure 5). Indeed, the differential capacity profiles for **1** display increased asymmetry in the low-potential region over the course of electrochemical cycling. By cycle 50, the reductive feature near 2.25 V and the oxidative shoulder near 2.5 V are substantially diminished, suggesting slight irreversibility at the highest levels of reduction. Changes in the conductivity of **1** at full reduction may contribute to this irreversibility, as well as interfaces formed by tetrafluoroborate-based electrolytes that are known to alter the cycling stability of cathode materials. Given the localized electronic structure of these states, the loss of capacity may also relate to a polaronic distortion that limits the reversibility of the reduction or traps Li$^+$ ions coordinated to the framework. Importantly, the electrolyte solution remained colorless following cycling

experiments, suggesting that framework dissolution does not occur during the course of electrochemical cycling, in contrast to other high-capacity coordination solids proposed as candidate cathode materials.[11a]

We note that all capacity and energy density values reported here for **1** and **2-SO$_4$** are calculated based on the masses of the as-synthesized framework materials, which include dimethylammonium cations. Accounting for only the mass of the host lattice, as is typical for metal−organic frameworks, the specific capacity and energy of **1** are 220 mAh/g and 600 Wh/kg, respectively. Furthermore, the chloride substituents in **1** do not contribute to the electrochemical capacity; thus, substitution of the Cl$_2$ dhbq^{n-} ligands with dhbq^{n-} or F$_2$ dhbq^{n-} could further boost the capacity of **1** to above 300 mAh/g.[32] While our attempts to synthesize the nonchlorinated analogues of **1** have not yet yielded the isostructural phases, we expect that the redox activity observed here could easily be extended to framework-based cathodes with capacities and energy densities that surpass those of state-of-the-art cathode materials (Figure S19).

Ion Insertion Mechanism. Given that most metal−organic frameworks are electronic insulators, electron transport to redox-active sites is often assumed to be the rate-limiting factor in their performance as cathode materials. In poorly conductive frameworks such as **2-SO$_4$**, this assumption likely holds. However, in more conductive frameworks such as **1**, ion transport can become a larger barrier to achieving fast charging rates. Ion transport in microporous materials is still poorly understood and is highly dependent on the pore environment of the material. While designing frameworks possessing large charge capacities and high conductivities is alone challenging, understanding the mechanism and rate of ion transport through framework-based cathode materials represents an equally important challenge. Ideally, the negatively charged framework would act as a weakly coordinating network that enables low-barrier cation transport in the pore, although previous studies on ion transport in metal−organic frameworks suggest this is not the case.[8a] Unlike dense solid-state materials, where the alkali metal cation is the lone mobile species, microporous materials may possess complex mobile species involving cations, anions, and solvent molecules, and nano-confinement of these species further complicates transport processes.[33] Moreover, cathode reduction may involve a mixture of cation insertion and anion deinsertion, and the mobile species may change over the course of electrochemical cycling.[34] This uncertainty hinders the ability to design porous cathode materials with optimized electronic and ionic transport, particularly for multivalent cations.[9a,31] For example, both **1** and **2-SO$_4$** display large voltage hysteresis between charging and discharging (Figures 5a and S16), despite the absence of a structural transformation. At higher potentials, this polarization is largely independent of charging rate, while a pronounced increase in polarization voltage is observed at low potentials with increased charging rates. Understanding the mechanism of this polarization is critical for obtaining improved performance in framework-based cathodes.

In order to better understand the nature of the mobile ionic species in **1**, we explored the cation and anion dependence of its electrochemical performance (Figure 6). If the primary mobile species are mononuclear alkali metal ions, then smaller cations are expected to display improved capacities and kinetics, with little dependence on the nature of the anion. In fact, pronounced dependences are observed for both the
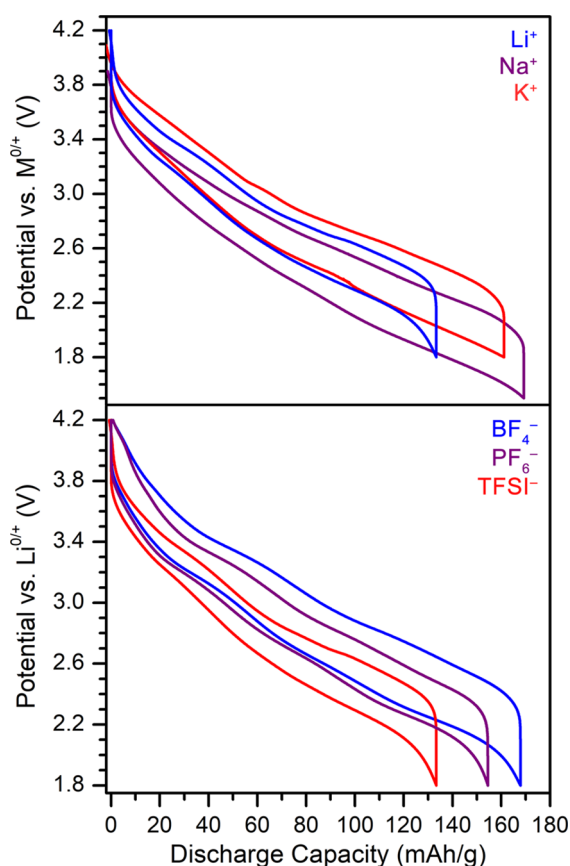
Figure 6. Cation (upper) and anion (lower) dependence of the discharge capacity for **1**. Discharge curves were collected with TFSI⁻ for the cation dependence and Li⁺ for the anion dependence. All curves shown represent the peak capacity achieved over 15 cycles.

cationic and anionic components of the electrolyte. Using the bis(trifluoromethanesulfonyl)imide (TFSI⁻) salts of Li⁺, Na⁺, and K⁺, **1** displays the largest capacity with sodium, followed by potassium and lithium. However, lithium displays a smaller polarization than the larger metal ions. Similarly, the BF_4^- anion displays the largest capacity, followed by PF_6^- and TFSI⁻. The anion dependence of the capacity tracks with the size of the anion, suggesting anions present in the pores of **1** may reduce the ionic mobility.

In all cases shown here, the voltage hysteresis between charging and discharging is substantially larger near full reduction, which can possibly be attributed to two primary factors. First, the highly anionic framework should interact more strongly with cations, hindering their ability to move within the pores. Second, the fully reduced framework could experience pore clogging as additional solvated cations insert into the framework. While these initial studies highlight that ion transport in metal−organic frameworks cannot be modeled as simple diffusion of solvated cations, they do not address the nature of the mobile species or entirely explain the observed cation and anion dependences. Further investigations aimed to address these points will be the focus of future work. Additionally, these results highlight the versatility of metal−organic frameworks cathodes, as similar capacities are obtained for a range of battery chemistries.

Beyond this electrolyte dependence, we note that the insertion mechanism of **1** is particularly unusual in that electron and ion transport are not dimensionally coupled.

Electron transport is expected to be two-dimensional along the *ab*-plane, with little contribution from interlayer charge hopping. In contrast, ion transport is expected to occur through the one-dimensional pores along the *c*-axis, which is perpendicular to the direction of electron transport. This mismatch between electron and ion transport is highly unusual in cathode materials, and its effect on the electrochemical data presented here is not immediately evident.

CONCLUSIONS

The foregoing results demonstrate that combined metal- and linker-centered redox chemistry can be utilized in the metal−organic framework materials **1** and **2-SO₄** to realize electrochemical capacities rivaling those of traditional cathode materials. The spectroscopic and electrochemical data presented demonstrate that the adjacent reduction potentials for iron and chloranilate are critical for accessing the exceptional capacity in these frameworks, while electronic structure calculations illustrate the comparable energies of metal and ligand reduction. The combination of conductivity, porosity, and metal-linker covalency in **1** gives rise to energy densities up to 533 Wh/kg and high charge capacity retention at charging rates up to 150 mA/g. While further enhancement of capacity and discharge potential are required for framework materials to compete with inorganic cathodes, these results suggest that the design of new framework-based cathode materials should focus on identifying new metal−organic linker pairings that may feature similar bonding interactions, using combined computational and experimental screening. Such an approach could lead not only to the identification of new cathode materials, but also to the discovery frameworks that can stabilize highly reduced organic species through covalent interactions. Indeed, reduced forms of **1** may display improved conductivity or interesting magnetic properties, and efforts are now underway to isolate and study chemically reduced samples. Finally, the cation and anion dependence of the electrochemical behavior shown here make apparent the need for improved understanding of ion transport in crystalline microporous solids.

While metal−organic framework cathodes could potentially be applied to next-generation battery technologies, particularly those using multivalent cations, it is first necessary to identify the effects of pore size and environment on ion transport. Larger pores, higher electrolyte concentrations, and chelating polyether solvents may screen cation-framework interactions to promote rapid diffusion through the pore.[35] Framework pores specifically designed to limit these interactions would greatly enhance the potential of these materials in fast-charging and high power energy storage applications. The continued development of metal−organic framework-based cathodes will rely on improved understanding of the electronic and ionic transport behavior of these materials.

EXPERIMENTAL SECTION

Synthesis of $(H_2NMe_2)_2Fe_2(Cl_2\,dhbq)_3(DMF)_{0.4}$ (1). In a round-bottom flask, a solution of chloranilic acid (257 mg) and dimethylamine (171 μL of a 0.2 M aqueous solution) in 6 mL of DMF was sparged with Ar for 15 min. A separate, freshly prepared aqueous solution of 1 M $Fe(NO_3)_3$ (10 mL) was sparged with Ar for 15 min. In air, 140 μL of the $Fe(NO_3)_3$ solution was quickly added to 1.4 mL of the DMF solution in a thick-walled borosilicate tube. The reaction mixture was degassed with three freeze−pump−thaw cycles, and then the tube was flame-sealed and placed in an oven preheated

to 120 °C. After 18 h, the tube was removed from the oven and allowed to cool to ambient temperature. The resulting black powder was filtered inside a vacuum atmospheres glovebox with a humid N_2 atmosphere, and was then transferred to an MBraun glovebox with a dry Ar atmosphere. The crude product was soaked in 10 mL of DMF for 24 h, and then the supernatant was decanted and replaced with fresh DMF. This washing procedure was repeated two more times, and then the solid was filtered and rinsed with 1 mL of THF. The DMF-solvated material was then soaked in 10 mL of THF at 50 °C for 48 h, during which time the solvent was replaced with fresh THF three times. The material was then activated at 120 °C under reduced pressure to afford **1** as a black powder. Yield: 15 mg (26%). Anal. Calcd for $C_{23.2}Cl_6Fe_2H_{18.8}N_{2.4}O_{12.4}$: C, 32.6; H, 2.2; N, 3.9. Found: C, 32.5; H, 2.3; N, 4.2. For spectroscopic and electrochemical experiments, many individual batches of the material were synthesized separately and combined for washing, activation, and characterization. IR (solid-ATR): 2786 (w), 1655 (s), 1478 (s), 1340 (s), 1251 (m), 1224 (m), 1190 (w), 1094 (m), 1060 (m), 1021 (m), 962 (w), 830 (w), 661 (m), and 488 (m) cm^{-1}.

Synthesis of $(H_2NMe_2)_4Fe_3(Cl_2 dhbq)_3(SO_4)_2(DMF)_{1.4}(THF)_{1.0}$ (2-SO$_4$). Under Ar, 100 mL of anhydrous, degassed DMF was added to a flame-dried Schlenk flask. To this flask was added chloranilic acid (168 mg, 0.800 mmol) and $FeSO_4·7H_2O$ (345 mg, 1.24 mmol). The reaction was heated to 130 °C with stirring for 24 h. The reaction was subsequently allowed to cool, and the black solid was allowed to settle to the bottom of the flask. The DMF was decanted and then replaced with 50 mL of fresh DMF. This washing procedure was repeated two more times, and then the flask was transferred to an Ar-filled glovebox. The microcrystalline powder was then filtered and rinsed with THF, and then soaked in 10 mL of THF at 50 °C for 48 h, during which time the solvent was replaced with fresh THF three times. The material was then activated at 120 °C under reduced pressure to afford **2-SO$_4$** as a black powder. Yield: 124 mg (34%). Anal. Calcd for $C_{34.5}Cl_6Fe_3H_{50.5}N_{5.4}O_{22.5}S_2$: C, 30.8; H, 3.8; N, 5.6; S, 4.7. Found: C, 31.3; H, 3.4; N, 5.7; S, 4.3. IR (solid-ATR) 1508 (s), 1483 (s), 1351 (m), 1315 (s), 1182 (w), 1052 (s), 999 (s), 899 (w), 854 (m), 642 (w), 573 (s), 508 (m) cm^{-1}.

Preparation of Single Crystals of Solvated $(H_2NMe_2)_4Fe_3(Cl_2 dhbq)_3(SO_4)_2$ (2-SO$_4$). A thick-walled borosilicate tube was charged with $FeSO_4·7H_2O$ (12 mg, 0.041 mmol), chloranilic acid (5.6 mg, 0.027 mmol), and anhydrous DMF (3 mL). The purple solution was degassed with three freeze−pump−thaw cycles, and the tube was sealed under vacuum. The reaction was heated to 120 °C for 24 h, and was then allowed to cool to ambient temperature to yield black, hexagonal single crystals of solvated **2-SO$_4$**.

Computational Details. Periodic DFT calculations were performed without any symmetry constraints using the Vienna ab initio Simulation Package (VASP).[36] During the geometry optimizations, both atomic positions and the lattice parameters were allowed to relax. We employed the PBE[37] exchange−correlation functional plus U method with 520 eV plane-wave cutoff (further discussion of the choice of U is included in the SI). A Hellman−Feynman force criterion of 0.05 eV/Å was used on each relaxed ion. For the electronic minimization, we used a convergence criterion of 10^{-6} eV. The core−valence electron interactions were described by using the projector augmented wave (PAW) method[38] with H (1s), C (2s, 2p), O (2s, 2p), Cl (3s, 3p), Fe (4s, 3d), and Cr (4s, 3d) electrons being treated as valence states. Dispersion effects were included through the D3-correction[39] with Becke-Johnson damping.[40] A $1 \times 1 \times 2$ k-point mesh was used for the sampling of the first Brillouin zone[41] during geometry optimization (see Table S3 for k-point mesh convergence).

ASSOCIATED CONTENT

Ⓢ Supporting Information

The Supporting Information is available free of charge at https://pubs.acs.org/doi/10.1021/jacs.9b13050.

Additional experimental details; powder X-ray diffraction data; electronic conductivity data; infrared, UV−vis−

NIR, and Mössbauer spectroscopy; computational details; electrochemical data; and additional references (PDF)

Crystallographic data (CIF)

AUTHOR INFORMATION

Corresponding Author

Jeffrey R. Long − *Department of Chemistry and Department of Chemical and Biomolecular Engineering, University of California, Berkeley, California 94720, United States; Materials Sciences Division, Lawrence Berkeley National Laboratory, Berkeley, California 94720, United States;* ⓘ orcid.org/0000-0002-5324-1321; Email: jrlong@berkeley.edu

Authors

Michael E. Ziebel − *Department of Chemistry, University of California, Berkeley, California 94720, United States; Materials Sciences Division, Lawrence Berkeley National Laboratory, Berkeley, California 94720, United States;* ⓘ orcid.org/0000-0003-1857-8292

Carlo Alberto Gaggioli − *Department of Chemistry, Chemical Theory Center and Supercomputing Institute, University of Minnesota, Minneapolis, Minnesota 55455, United States;* ⓘ orcid.org/0000-0001-9105-8731

Ari B. Turkiewicz − *Department of Chemistry, University of California, Berkeley, California 94720, United States*

Won Ryu − *Department of Chemical and Biomolecular Engineering, University of California, Berkeley, California 94720, United States*

Laura Gagliardi − *Department of Chemistry, Chemical Theory Center and Supercomputing Institute, University of Minnesota, Minneapolis, Minnesota 55455, United States;* ⓘ orcid.org/0000-0001-5227-1396

Complete contact information is available at:
https://pubs.acs.org/10.1021/jacs.9b13050

Notes

The authors declare no competing financial interest.

ACKNOWLEDGMENTS

discussions and experimental assistance; Dr. T. David Harris for helpful discussions; and Dr. Katie R. Meihaus for editorial assistance.

■ REFERENCES

(1) (a) Mizushima, K.; Jones, P.; Wiseman, P.; Goodenough, J. Li_xCoO_2 ($0 < x \leq 1$): A New Cathode Material for Batteries of High Energy Density. *Solid State Ionics* **1981**, *3–4*, 171–174. (b) Padhi, A. K.; Nanjundaswamy, K. S.; Goodenough, J. B. Phospho-olivines as Positive-Electrode Materials for Rechargeable Lithium Batteries. *J. Electrochem. Soc.* **1997**, *144*, 1188–1194.

(2) (a) Lu, Z.; Dahn, J. R. Understanding the Anomalous Capacity of $Li/Li[Ni_xLi_{(1/3−2x/3)}]Mn_{(2/3−x/3)}O_2$ Cells Using *In Situ* X-Ray Diffraction and Electrochemical Studies. *J. Electrochem. Soc.* **2002**, *149*, A815–A822. (b) Sathiya, M.; Rousse, G.; Ramesha, K.; Laisa, C. P.; Vezin, H.; Sougrati, M. T.; Doublet, M. L.; Foix, D.; Gonbeau, D.; Walker, W.; Prakash, A. S.; Ben Hassine, M.; Dupont, L.; Tarascon, J. M. Reversible Anionic Redox Chemistry in High-Capacity Layered-Oxide Electrodes. *Nat. Mater.* **2013**, *12*, 827–835. (c) Yabuuchi, N.; Takeuchi, M.; Nakayama, M.; Shiiba, H.; Ogawa, M.; Nakayama, K.; Ohta, T.; Endo, D.; Ozaki, T.; Inamasu, T.; Sato, K.; Komaba, S. High-Capacity Electrode Materials for Rechargeable Lithium Batteries: Li_3NbO_4-Based System with Cation-Disordered Rocksalt Structure. *Proc. Natl. Acad. Sci. U. S. A.* **2015**, *112*, 7650–7655. (d) Luo, K.; Roberts, M. R.; Hao, R.; Guerrini, N.; Pickup, D. M.; Liu, Y. S.; Edstrom, K.; Guo, J.; Chadwick, A. V.; Duda, L. C.; Bruce, P. G. Charge-Compensation in 3d-Transition-Metal-Oxide Intercalation Cathodes Through the Generation of Localized Electron Holes on Oxygen. *Nat. Chem.* **2016**, *8*, 684–691. (e) Perez, A. J.; Jacquet, Q.; Batuk, D.; Iadecola, A.; Saubanère, M.; Rousse, G.; Larcher, D.; Vezin, H.; Doublet, M.-L.; Tarascon, J.-M. Approaching the Limits of Cationic and Anionic Electrochemical Activity with the Li-Rich Layered Rocksalt Li_3IrO_4. *Nat. Energy* **2017**, *2*, 954–962.

(3) (a) McCalla, E.; Sougrati, M. T.; Rousse, G.; Berg, E. J.; Abakumov, A.; Recham, N.; Ramesha, K.; Sathiya, M.; Dominko, R.; Van Tendeloo, G.; Novak, P.; Tarascon, J. M. Understanding the Roles of Anionic Redox and Oxygen Release During Electrochemical Cycling of Lithium-Rich Layered Li_4FeSbO_6. *J. Am. Chem. Soc.* **2015**, *137*, 4804–4814. (b) McCalla, E.; Prakash, A. S.; Berg, E.; Saubanère, M.; Abakumov, A. M.; Foix, D.; Klobes, B.; Sougrati, M.-T.; Rousse, G.; Lepoivre, F.; Mariyappan, S.; Doublet, M. L.; Gonbeau, D.; Novak, P.; Van Tendeloo, G.; Hermann, R. P.; Tarascon, J.-M. Reversible Li-Intercalation through Oxygen Reactivity in Li-Rich Li-Fe-Te Oxide Materials. *J. Electrochem. Soc.* **2015**, *162*, A1341–A1351.

(4) (a) Croy, J. R.; Gallagher, K. G.; Balasubramanian, M.; Chen, Z.; Ren, Y.; Kim, D.; Kang, S.-H.; Dees, D. W.; Thackeray, M. M. Examining Hysteresis in Composite $x Li_2MnO_3 \cdot (1-x)LiMO_2$ Cathode Structures. *J. Phys. Chem. C* **2013**, *117*, 6525–6536. (b) Rinaldo, S. G.; Gallagher, K. G.; Long, B. R.; Croy, J. R.; Bettge, M.; Abraham, D. P.; Bareño, J.; Dees, D. W. Physical Theory of Voltage Fade in Lithium-and Manganese-Rich Transition Metal Oxides. *J. Electrochem. Soc.* **2015**, *162*, A897–A904. (c) Assat, G.; Delacourt, C.; Corte, D. A. D.; Tarascon, J.-M. Practical Assessment of Anionic Redox in Li-Rich Layered Oxide Cathodes: A Mixed Blessing for High Energy Li-Ion Batteries. *J. Electrochem. Soc.* **2016**, *163*, A2965–A2976. (d) Zheng, J.; Myeong, S.; Cho, W.; Yan, P.; Xiao, J.; Wang, C.; Cho, J.; Zhang, J.-G. Li-and Mn-Rich Cathode Materials: Challenges to Commercialization. *Adv. Energy Mater.* **2017**, *7*, 1601284. (e) Assat, G.; Foix, D.; Delacourt, C.; Iadecola, A.; Dedryvere, R.; Tarascon, J. M. Fundamental Interplay Between Anionic/Cationic Redox Governing the Kinetics and Thermodynamics of Lithium-Rich Cathodes. *Nat. Commun.* **2017**, *8*, 2219.

(5) (a) Rozier, P.; Tarascon, J. M. Li-Rich Layered Oxide Cathodes for Next-Generation Li-Ion Batteries: Chances and Challenges. *J. Electrochem. Soc.* **2015**, *162*, A2490–A2499. (b) Assat, G.; Tarascon, J.-M. Fundamental Understanding and Practical Challenges of Anionic Redox Activity in Li-Ion Batteries. *Nat. Energy* **2018**, *3*, 373–386.

(6) (a) Long, J. R.; Yaghi, O. M. The Pervasive Chemistry of Metal-Organic Frameworks. *Chem. Soc. Rev.* **2009**, *38*, 1213–1214. (b) Zhou, H. C.; Kitagawa, S. Metal-Organic Frameworks (MOFs). *Chem. Soc. Rev.* **2014**, *43*, 5415–5418.

(7) Ferey, G.; Millange, F.; Morcrette, M.; Serre, C.; Doublet, M. L.; Greneche, J. M.; Tarascon, J. M. Mixed-Valence Li/Fe-Based Metal-Organic Frameworks with Both Reversible Redox and Sorption Properties. *Angew. Chem., Int. Ed.* **2007**, *46*, 3259–3263.

(8) (a) Wiers, B. M.; Foo, M. L.; Balsara, N. P.; Long, J. R. A Solid Lithium Electrolyte via Addition of Lithium Isopropoxide to a Metal-Organic Framework with Open Metal Sites. *J. Am. Chem. Soc.* **2011**, *133*, 14522–14525. (b) Horike, S.; Umeyama, D.; Kitagawa, S. Ion Conductivity and Transport by Porous Coordination Polymers and Metal-Organic Frameworks. *Acc. Chem. Res.* **2013**, *46*, 2376–2384. (c) Park, S. S.; Tulchinsky, Y.; Dinca, M. Single-Ion Li^+, Na^+, and Mg^{2+} Solid Electrolytes Supported by a Mesoporous Anionic Cu-Azolate Metal-Organic Framework. *J. Am. Chem. Soc.* **2017**, *139*, 13260–13263.

(9) (a) Aubrey, M. L.; Long, J. R. A Dual-Ion Battery Cathode via Oxidative Insertion of Anions in a Metal-Organic Framework. *J. Am. Chem. Soc.* **2015**, *137*, 13594–13602. (b) Song, J.; Sahadeo, E.; Noked, M.; Lee, S. B. Mapping the Challenges of Magnesium Battery. *J. Phys. Chem. Lett.* **2016**, *7*, 1736–1749.

(10) Zhang, Z.; Yoshikawa, H.; Awaga, K. Monitoring the Solid-State Electrochemistry of Cu(2,7-AQDC) (AQDC = Anthraquinone Dicarboxylate) in a Lithium Battery: Coexistence of Metal and Ligand Redox Activities in a Metal-Organic Framework. *J. Am. Chem. Soc.* **2014**, *136*, 16112–16115.

(11) (a) Fang, C.; Huang, Y.; Yuan, L.; Liu, Y.; Chen, W.; Huang, Y.; Chen, K.; Han, J.; Liu, Q.; Huang, Y. A Metal-Organic Compound as Cathode Material with Superhigh Capacity Achieved by Reversible Cationic and Anionic Redox Chemistry for High-Energy Sodium-Ion Batteries. *Angew. Chem., Int. Ed.* **2017**, *56*, 6793–6797. (b) Dühnen, S.; Nölle, R.; Wrogemann, J.; Winter, M.; Placke, T. Reversible Anion Storage in a Metal-Organic Framework for Dual-Ion Battery Systems. *J. Electrochem. Soc.* **2019**, *166*, A5474–A5482.

(12) Park, J.; Lee, M.; Feng, D.; Huang, Z.; Hinckley, A. C.; Yakovenko, A.; Zou, X.; Cui, Y.; Bao, Z. Stabilization of Hexaaminobenzene in a 2D Conductive Metal-Organic Framework for High Power Sodium Storage. *J. Am. Chem. Soc.* **2018**, *140*, 10315–10323.

(13) (a) D'Alessandro, D. M. Exploiting Redox Activity in Metal-Organic Frameworks: Concepts, Trends and Perspectives. *Chem. Commun.* **2016**, *52*, 8957–8971. (b) Walsh, A.; Butler, K. T.; Hendon, C. H. Chemical Principles for Electroactive Metal-Organic Frameworks. *MRS Bull.* **2016**, *41*, 870–876. (c) Sun, L.; Campbell, M. G.; Dinca, M. Electrically Conductive Porous Metal-Organic Frameworks. *Angew. Chem., Int. Ed.* **2016**, *55*, 3566–3579.

(14) (a) Nguyen, T. L. A.; Demir-Cakan, R.; Devic, T.; Morcrette, M.; Ahnfeldt, T.; Auban-Senzier, P.; Stock, N.; Goncalves, A. M.; Filinchuk, Y.; Tarascon, J. M.; Ferey, G. 3-D Coordination Polymers Based on the Tetrathiafulvalenetetracarboxylate (TTF-TC) Derivative: Synthesis, Characterization, and Oxidation Issues. *Inorg. Chem.* **2010**, *49*, 7135–7143. (b) Wade, C. R.; Li, M.; Dinca, M. Facile Deposition of Multicolored Electrochromic Metal-Organic Framework Thin Films. *Angew. Chem., Int. Ed.* **2013**, *52*, 13377–13381. (c) Zhang, Z.; Yoshikawa, H.; Awaga, K. Discovery of a "Bipolar Charging" Mechanism in the Solid-State Electrochemical Process of a Flexible Metal-Organic Framework. *Chem. Mater.* **2016**, *28*, 1298–1303. (d) Celis-Salazar, P. J.; Epley, C. C.; Ahrenholtz, S. R.; Maza, W. A.; Usov, P. M.; Morris, A. J. Proton-Coupled Electron Transport in Anthraquinone-Based Zirconium Metal-Organic Frameworks. *Inorg. Chem.* **2017**, *56*, 13741–13747. (e) Goswami, S.; Nelson, J. N.; Islamoglu, T.; Wu, Y.-L.; Farha, O. K.; Wasielewski, M. R. Photoexcited Naphthalene Diimide Radical Anion Linking the Nodes of a Metal-Organic Framework: A Heterogeneous Super-Reductant. *Chem. Mater.* **2018**, *30*, 2488–2492.

(15) (a) Shilov, G. V.; Nikitina, Z. K.; Ovanesyan, N. S.; Aldoshin, S. M.; Makhaev, V. D. Phenazineoxonium Chloranilatomanganate and

Chloranilatoferrate: Synthesis, Structure, Magnetic Properties, and Mössbauer Spectra. *Russ. Chem. Bull.* **2011**, *60*, 1209−1219. (b) Darago, L. E.; Aubrey, M. L.; Yu, C. J.; Gonzalez, M. I.; Long, J. R. Electronic Conductivity, Ferrimagnetic Ordering, and Reductive Insertion Mediated by Organic Mixed-Valence in a Ferric Semiquinoid Metal-Organic Framework. *J. Am. Chem. Soc.* **2015**, *137*, 15703−15711. (c) DeGayner, J. A.; Jeon, I.-R.; Sun, L.; Dinca, M.; Harris, T. D. 2D Conductive Iron-Quinoid Magnets Ordering up to *T*$_c$ = 105 K via Heterogeneous Redox Chemistry. *J. Am. Chem. Soc.* **2017**, *139*, 4175−4184. (d) Benmansour, S.; Abherve, A.; Gomez-Claramunt, P.; Valles-Garcia, C.; Gomez-Garcia, C. J. Nanosheets of Two-Dimensional Magnetic and Conducting Fe(II)/Fe(III) Mixed-Valence Metal-Organic Frameworks. *ACS Appl. Mater. Interfaces* **2017**, *9*, 26210−26218. (e) Murase, R.; Abrahams, B. F.; D'Alessandro, D. M.; Davies, C. G.; Hudson, T. A.; Jameson, G. N. L.; Moubaraki, B.; Murray, K. S.; Robson, R.; Sutton, A. L. Mixed Valency in a 3D Semiconducting Iron-Fluoranilate Coordination Polymer. *Inorg. Chem.* **2017**, *56*, 9025−9035. (f) Ziebel, M. E.; Darago, L. E.; Long, J. R. Control of Electronic Structure and Conductivity in Two-Dimensional Metal-Semiquinoid Frameworks of Titanium, Vanadium, and Chromium. *J. Am. Chem. Soc.* **2018**, *140*, 3040−3051. (g) Sahadevan, S. A.; Abherve, A.; Monni, N.; Saenz de Pipaon, C.; Galan-Mascaros, J. R.; Waerenborgh, J. C.; Vieira, B. J. C.; Auban-Senzier, P.; Pillet, S.; Bendeif, E.-E.; Alemany, P.; Canadell, E.; Mercuri, M. L.; Avarvari, N. Conducting Anilate-Based Mixed-Valence Fe(II)Fe(III) Coordination Polymer: Small-Polaron Hopping Model for Oxalate-Type Fe(II)Fe(III) 2D Networks. *J. Am. Chem. Soc.* **2018**, *140*, 12611−12621.

(16) Guo, D.; McCusker, J. K. Spin Exchange Effects on the Physicochemical Properties of Tetraoxolene-Bridged Bimetallic Complexes. *Inorg. Chem.* **2007**, *46*, 3257−3274.

(17) Jeon, I.-R.; Negru, B.; Van Duyne, R. P.; Harris, T. D. A 2D Semiquinone Radical-Containing Microporous Magnet with Solvent-Induced Switching from *T*$_c$ = 26 to 80 K. *J. Am. Chem. Soc.* **2015**, *137*, 15699−15702.

(18) Halis, S.; Inge, A. K.; Dehning, N.; Weyrich, T.; Reinsch, H.; Stock, N. Dihydroxybenzoquinone as Linker for the Synthesis of Permanently Porous Aluminum Metal-Organic Frameworks. *Inorg. Chem.* **2016**, *55*, 7425−7431.

(19) Nguyen, N. T.; Furukawa, H.; Gandara, F.; Trickett, C. A.; Jeong, H. M.; Cordova, K. E.; Yaghi, O. M. ThreeDimensional Metal-Catecholate Frameworks and Their Ultrahigh Proton Conductivity. *J. Am. Chem. Soc.* **2015**, *137*, 15394−15397.

(20) Brunschwig, B. S.; Creutz, C.; Sutin, N. Optical Transitions of Symmetrical Mixed-Valence Systems in the Class II-III Transition Regime. *Chem. Soc. Rev.* **2002**, *31*, 168−184.

(21) Taniguchi, K.; Chen, J.; Sekine, Y.; Miyasaka, H. Magnetic Phase Switching in a Tetraoxolene-Bridged Honeycomb Ferrimagnet Using a Lithium Ion Battery System. *Chem. Mater.* **2017**, *29*, 10053−10059.

(22) D'Alessandro, D. M.; Keene, F. R. A Cautionary Warning on the Use of Electrochemical Measurements to Calculate Comproportionation Constants for Mixed-Valence Compounds. *Dalton Trans.* **2004**, 3950−3954.

(23) Abrahams, B. F.; Bond, A. M.; Le, T. H.; McCormick, L. J.; Nafady, A.; Robson, R.; Vo, N. Voltammetric Reduction and Re-Oxidation of Solid Coordination Polymers of Dihydroxybenzoquinone. *Chem. Commun.* **2012**, *48*, 11422−11424.

(24) Chen, J.; Taniguchi, K.; Sekine, Y.; Miyasaka, H. Electrochemical Development of Magnetic Long-Range Correlations with *T*$_c$ = 128 K in a Tetraoxolene-Bridged Fe-Based Framework. *J. Magn. Magn. Mater.* **2020**, *494*, 165818.

(25) Dei, A.; Gatteschi, D.; Pardi, L.; Russo, U. Tetraoxolene Radical Stabilization by the Interaction with Transition-Metal Ions. *Inorg. Chem.* **1991**, *30*, 2589−2594.

(26) (a) Yoon, W.-S.; Kim, K.-B.; Kim, M.-G.; Lee, M. K.; Shin, H.-J.; Lee, J.-M.; Lee, J.-S.; Yo, C.-H. Oxygen Contribution on Li-Ion Intercalation-Deintercalation in LiCoO$_2$ Investigated by O *K*-Edge and Co *L*-Edge X-ray Absorption Spectroscopy. *J. Phys. Chem. B*

2002, *106*, 2526−2532. (b) Goodenough, J. B.; Kim, Y. Challenges for Rechargeable Li Batteries. *Chem. Mater.* **2010**, *22*, 587−603.

(27) Krukau, A. V.; Vydrov, O. A.; Izmaylov, A. F.; Scuseria, G. E. Influence of the Exchange Screening Parameter on the Performance of Screened Hybrid Functionals. *J. Chem. Phys.* **2006**, *125*, 224106.

(28) Larcher, D.; Tarascon, J. M. Towards Greener and More Sustainable Batteries for Electrical Energy Storage. *Nat. Chem.* **2015**, *7*, 19−29.

(29) (a) Shin, J.; Kim, M.; Cirera, J.; Chen, S.; Halder, G. J.; Yersak, T. A.; Paesani, F.; Cohen, S. M.; Meng, Y. S. MIL-101(Fe) as a Lithium-Ion Battery Electrode Material: A Relaxation and Intercalation Mechanism During Lithium Insertion. *J. Mater. Chem. A* **2015**, *3*, 4738−4744. (b) Du, Z. Q.; Li, Y.-P.; Wang, X.-X.; Wang, J.; Zhai, Q.-G. Enhanced Electrochemical Performance of Li-Co-BTC Ternary Metal-Organic Frameworks as Cathode Materials for Lithium-Ion Batteries. *Dalton Trans.* **2019**, *48*, 2013−2018.

(30) Amatucci, G. G.; Tarascon, J. M.; Klein, L. C. CoO$_2$, The End Member of the Li$_x$CoO$_2$ Solid Solution. *J. Electrochem. Soc.* **1996**, *143*, 1114−1123.

(31) Wada, K.; Sakaushi, K.; Sasaki, S.; Nishihara, H. Multielectron-Transfer-based Rechargeable Energy Storage of Two-Dimensional Coordination Frameworks with Non-Innocent Ligands. *Angew. Chem., Int. Ed.* **2018**, *57*, 8886−8890.

(32) Kingsbury, C. J.; Abrahams, B. F.; D'Alessandro, D. M.; Hudson, T. A.; Murase, R.; Robson, R.; White, K. F. Role of NEt$_4^+$ in Orienting and Locking Together [M$_2$ lig$_3$]$^{2-}$ (6,3) Sheets (H$_2$ lig = Chloranilic or Fluoranilic Acid) to Generate Spacious Channels Perpendicular to the Sheets. *Cryst. Growth Des.* **2017**, *17*, 1465−1470.

(33) (a) Liu, L.; Chen, X.; Lu, W.; Han, A.; Qiao, Y. Infiltration of Electrolytes in Molecular-Sized Nanopores. *Phys. Rev. Lett.* **2009**, *102*, 184501. (b) Zwolak, M.; Lagerqvist, J.; Di Ventra, M. Quantized Ionic Conductance in Nanopores. *Phys. Rev. Lett.* **2009**, *103*, 128102. (c) Wang, H.; Forse, A. C.; Griffin, J. M.; Trease, N. M.; Trognko, L.; Taberna, P. L.; Simon, P.; Grey, C. P. In Situ NMR Spectroscopy of Supercapacitors: Insight into the Charge Storage Mechanism. *J. Am. Chem. Soc.* **2013**, *135*, 18968−18980.

(34) (a) Griffin, J. M.; Forse, A. C.; Wang, H.; Trease, N. M.; Taberna, P. L.; Simon, P.; Grey, C. P. Ion Counting in Supercapacitor Electrodes Using NMR Spectroscopy. *Faraday Discuss.* **2014**, *176*, 49−68. (b) Forse, A. C.; Merlet, C.; Griffin, J. M.; Grey, C. P. New Perspectives on the Charging Mechanisms of Supercapacitors. *J. Am. Chem. Soc.* **2016**, *138*, 5731−5744. (c) Forse, A. C.; Griffin, J. M.; Merlet, C.; Carretero-Gonzalez, J.; Raji, A.-R. O.; Trease, N. M.; Grey, C. P. Direct Observation of Ion Dynamics in Supercapacitor Electrodes Using In Situ Diffusion NMR Spectroscopy. *Nat. Energy* **2017**, *2* DOI: 10.1038/nenergy.2016.216.

(35) (a) Largeot, C.; Portet, C.; Chmiola, J.; Taberna, P. L.; Gogotsi, Y.; Simon, P. Relation Between the Ion Size and Pore Size for an Electric Double-Layer Capacitor. *J. Am. Chem. Soc.* **2008**, *130*, 2730−2731. (b) Richey, F. W.; Tran, C.; Kalra, V.; Elabd, Y. A. Ionic Liquid Dynamics in Nanoporous Carbon Nanofibers in Supercapacitors Measured with in Operando Infrared Spectroelectrochemistry. *J. Phys. Chem. C* **2014**, *118*, 21846−21855.

(36) (a) Kresse, G.; Hafner, J. *Ab initio* Molecular-Dynamics Simulation of the Liquid-Metal-Amorphous-Semiconductor Transition in Germanium. *Phys. Rev. B: Condens. Matter Mater. Phys.* **1994**, *49*, 14251−14269. (b) Kresse, G.; Furthmüller, J. Efficiency of Ab-Initio Total Energy Calculations for Metals and Semiconductors Using a Plane-Wave Basis Set. *Comput. Mater. Sci.* **1996**, *6*, 15−50.

(37) Perdew, J. P.; Burke, K.; Ernzerhof, M. Generalized Gradient Approximation Made Simple. *Phys. Rev. Lett.* **1996**, *77*, 3865−3868.

(38) Blöchl, P. E. Projector Augmented-Wave Method. *Phys. Rev. B: Condens. Matter Mater. Phys.* **1994**, *50*, 17953−17979.

(39) Grimme, S.; Antony, J.; Ehrlich, S.; Krieg, H. A Consistent and Accurate Ab Initio Parametrization of Density Functional Dispersion Correction (DFT-D) for the 94 Elements H-Pu. *J. Chem. Phys.* **2010**, *132*, 154104.

(40) Grimme, S.; Ehrlich, S.; Goerigk, L. Effect of the Damping Function in Dispersion Corrected Density Functional Theory. *J. Comput. Chem.* **2011**, *32*, 1456−1465.

(41) Monkhorst, H. J.; Pack, J. D. Special Points for Brillouin-Zone Integrations. *Phys. Rev. B* **1976**, *13*, 5188−5192.